Atmospheric Environment 373 (2026) 121896

Contents lists available at ScienceDirect

Atmospheric Environment

journal homepage: www.elsevier.com/locate/atmosenv

OH-initiated aqueous oxidation of methylglyoxal: Implications for organic acid and oligomer formation

Jiaxin Wang [a,b], Ying Chen [a,b], Wenjie Gao [a,b], Sihao Lin [a,b], Wenjian Li [a,b], Yongpeng Ji [a,b], Xiaolei Zhao [c], Yanpeng Gao [a,b], Yuemeng Ji [a,b,*], Taicheng An [a,b]

[a] Guangdong-Hong Kong-Macao Joint Laboratory for Contaminants Exposure and Health, Guangdong Key Laboratory of Environmental Catalysis and Health Risk Control, Institute Environmental Health and Pollution Control, Guangdong University of Technology, Guangzhou, 510006, China
[b] Guangdong Basic Research Center of Excellence for Ecological Security and Green Development, Key Laboratory of City Cluster Environmental Safety and Green Development of the Ministry of Education, School of Environmental Science and Engineering, Guangdong University of Technology, Guangzhou, 510006, China
[c] College of Chemistry and Chemical Engineering, Henan Key Laboratory of Coal Green Conversion, Henan Polytechnic University, Jiaozuo, 454000, China

HIGHLIGHTS

- Aqueous oxidation of MG readily occurs through its hydrated forms.
- H-abstraction pathway is of major importance in the OH-initiated oxidation.
- MG oxidation contributes to organic acids rather than oligomers in the atmosphere.
- Microdroplet acidity is enhanced by MG oxidation.

GRAPHICAL ABSTRACT

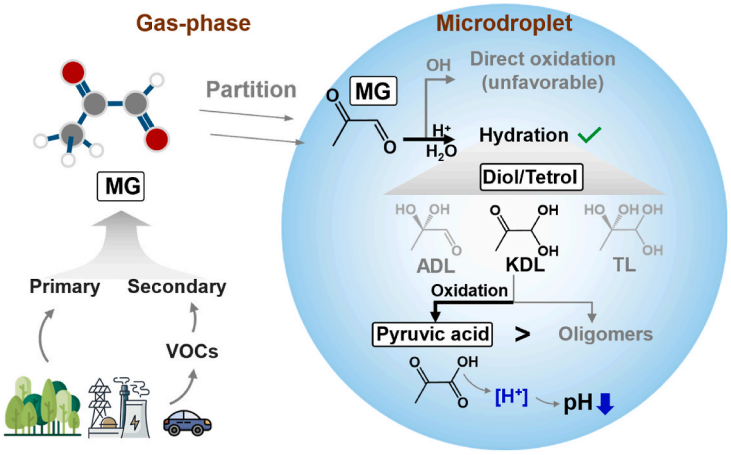

ARTICLE INFO

Keywords:
Methylglyoxal
Aqueous-phase oxidation
Reaction mechanisms
Organic acid
Microdroplet acidity

ABSTRACT

Multiphase chemistry of oxygenated volatile organic compounds (OVOCs) is a crucial route to form secondary organic aerosol. Hence, we investigated the aqueous oxidation mechanism and kinetics of methylglyoxal (MG), a representative OVOC, using quantum chemical calculations, kinetic rate analyses, and dynamic simulations. Our mechanism shows that, relative to direct oxidation of MG, aqueous oxidation of MG readily occurs via its hydrates such as diols and tetrol, which is dominated by H-abstraction pathways. Kinetic analysis reveals that the calculated rate constants for the OH-initiated reactions follow the ratio of KDL : TL : ADL ≈ 1 : 0.005 : 0.001, indicating that the OH-initiated KDL oxidation is of major importance in the atmosphere. Subsequent transformations mainly yield organic acids rather than oligomers under typical atmospheric conditions. Combined

* Corresponding author. Guangdong-Hong Kong-Macao Joint Laboratory for Contaminants Exposure and Health, Guangdong Key Laboratory of Environmental Catalysis and Health Risk Control, Institute Environmental Health and Pollution Control, Guangdong University of Technology, Guangzhou, 510006, China.
E-mail address: jiym@gdut.edu.cn (Y. Ji).

https://doi.org/10.1016/j.atmosenv.2026.121896
Received 3 December 2025; Received in revised form 24 January 2026; Accepted 21 February 2026
Available online 22 February 2026

with dynamic simulations, it can be found that pyruvic acid is the major product, and thus, microdroplet acidity is enhanced at the higher initial MG concentrations or under less acidic conditions. These results provide mechanistic and kinetic insights into the aqueous oxidation of MG and highlight its key role in organic acid formation. Our work underscores the importance of including the OVOC oxidation pathways when evaluating aqueous-phase chemistry and its impacts on aerosol acidity and composition.

1. Introduction

Multiphase reactions significantly contribute to atmospheric aerosols and fine particulate matter ($PM_{2.5}$), with profound implications for air quality, human health, and ecosystems (Fröhlich-Nowoisky et al., 2016; Ge et al., 2025; Lelieveld et al., 2020; Zhang et al., 2015). These processes typically occur on the surface or in the bulk of condensed matter, including liquid water and particles (Degefie et al., 2015; George et al., 2015; Li et al., 2020b; McNeill, 2015). Among these processes, aqueous-phase reactions of oxygenated volatile organic compounds (OVOCs) represent a crucial route, which affects the formation and composition of aerosols (Li et al., 2020a; Lim et al., 2010; McNeill, 2015). However, the mechanisms of some key aqueous processes of OVOCs remain unclear, highlighting the importance of further studies on aqueous-phase chemistry of OVOCs (McNeill, 2015; Tilgner et al., 2013).

Current studies on the aqueous-phase reactions of OVOCs have predominantly focused on acid-catalyzed chemical processes. Under acidic conditions, reactive OVOCs (e.g., carbonyl compounds) form high-molecular-weight products through protonation, hydration, and self-oligomerization, contributing to SOA formation (Chan et al., 2013; Ji et al., 2020; Ma et al., 2022). Besides, OVOCs also react with other dissolved species and thereby change the components of aerosols. For example, interactions between carbonyls and alcohols with sulfate anions (SO_4^{2-}) contribute to organosulfate formation (Minerath et al., 2008; Wang et al., 2023a, 2023b). Reactions of carbonyls with reduced nitrogen species (e.g., ammonium or amines) produce light-absorbing species such as imidazole and pyrrole compounds, contributing to brown carbon formation (Liu et al., 2024; Marrero-Ortiz et al., 2019; Powelson et al., 2014; Shi et al., 2024). In addition to acid-catalyzed pathways, aqueous oxidants can initiate the oxidation of OVOCs, forming organic acids or oligomers (Liu et al., 2012a; Schaefer et al., 2012; Zhang et al., 2010). Dicarbonyl compounds, such as methylglyoxal (MG) and glyoxal (GL), are abundant OVOCs in the atmosphere (Fu et al., 2008; Liu et al., 2012b). Their aqueous-phase oxidation has been widely investigated and shown to contribute significantly to the formation of organic acids and oligomers (Tan et al., 2010, 2012; Wei et al., 2023). Experimental and simulation studies further reveal the competition between oligomer and organic acid formation from dicarbonyl oxidation (Lim et al., 2013; Tan et al., 2009). For GL oxidation, glyoxylic and oxalic acids dominate at cloud-relevant GL concentrations (30 μM), while oligomer formation becomes more important at higher GL concentrations (3000 μM) (Tan et al., 2009). Similarly, for MG oxidation, oligomers significantly contribute to mass yields only when the MG concentration exceeds 10^{-2} M, while organic acids dominate when the MG concentration is in the range of 10^{-5} to 10^{-3} M (Lim et al., 2013). These findings reveal that the detailed mechanisms governing whether dicarbonyl oxidation forms oligomers or organic acids remain unclear. Hence, systematic studies of the aqueous oxidation of dicarbonyl compounds are needed to better illustrate the implications for aerosol particles.

In this study, the oxidation mechanisms and kinetics of dicarbonyl compounds are investigated in the aqueous phase using theoretical approach. Herein, MG is selected as a representative dicarbonyl compound due to its high atmospheric abundance and water solubility (Fu et al., 2008; Sander, 2015). The thermodynamic and kinetic properties for the initial transformation and oxidation of MG are explored using quantum chemical and kinetic rate calculations. The subsequent oxidation and oligomerization pathways are constructed. The product distributions are assessed by reaction dynamics modeling. Finally, the contribution of aqueous MG oxidation to oligomer and organic acid formation is evaluated, and the atmospheric implications are discussed.

2. Method

2.1. Electronic structure calculation

All quantum chemical calculations were performed using the Gaussian 09 program package (Frisch et al., 2009). Solvent effects were included via the solvation model based on density (SMD) (Marenich et al., 2009). The geometries of stationary points, including reactants, intermediates, transition states (TSs), and products, were optimized at the M06-2X/6-311G(d,p) level (Ji et al., 2017; Zhao et al., 2023; Zhao and Truhlar, 2008). Frequency analyses at the same level were carried out to confirm that each optimized structure corresponds to either a TS (with only one imaginary frequency) or the minima (without any imaginary frequencies). For reactions involving energy barriers, intrinsic reaction coordinate calculations were employed to confirm the reliable connection between TS and its corresponding reactants and products. In contrast, barrierless processes were characterized by scanning the potential energy profile along the relevant reaction coordinate using the relax scan method (Hazra and Sinha, 2011), with all other geometric parameters fully relaxed except for the breaking or forming bonds.

2.2. Energy refinement and kinetic calculation

Single-point energy refinements were performed at the M06-2X/6-311++G(3df,3pd) level (Li et al., 2024; Xu et al., 2019) to construct accurate potential energy surfaces (PESs). The dual-level approach is denoted as X//Y, representing that the geometry is optimized at the lower level Y, followed by a single-point energy calculation at the higher level X. The energy barrier ($\Delta G^{\ddagger}$) and the reaction energy (ΔG_r) are defined as $\Delta G^{\ddagger} = G_{TS} - G_{Reactants}$ and $\Delta G_r = G_{Products} - G_{Reactants}$, respectively, where G_{TS}, $G_{Reactants}$ and $G_{Products}$ represent the free energies of TS, reactants and products.

Based on the PES information, rate constants for pathways that have well-defined TSs were calculated using conventional transition-state theory (Henry, 1935) as follows (Evans and Polanyi, 1935; Eyring, 1935; Gao et al., 2013):

$$k_t = \sigma \frac{k_B T}{h} \exp\left(\frac{-\Delta G^{\ddagger}}{RT}\right) \quad (1)$$

where σ represents the reaction path degeneracy; k_B is Boltzmann constant, and h is Planck constant; $\Delta G^{\ddagger}$ is the free energy barrier obtained in PES data.

The effects of solvent cage confinement and molecular free volume were taken into account (Okuno, 1997):

$$\Delta G_s^{FV} \cong \Delta G_s^0 - RT\left\{\ln\left[n10^{(2n-2)}\right] - (n-1)\right\} \quad (2)$$

where n represents the number of molecules in reaction.

For bimolecular diffusion-controlled reactions, the effect of diffusion-limited conditions was considered, and the appearance rate constants k are calculated according to Collins-Kimball theory (Collins and Kimball, 1949) as follows:

$$k = \frac{k_t k_D}{k_t + k_D} \quad (3)$$

The steady-state rate constant (k_D) can be calculated as follows:

$$k_D = \frac{N_A k_B T \left(\frac{1}{r_a} + \frac{1}{r_b}\right) R_{AB}}{150\eta} \quad (4)$$

where r_a and r_b denote the radius of reactant A and B. For barrierless biomolecular reaction pathways, the rate constants are estimated using the k_D.

2.3. Reaction dynamic simulation

To simulate the degradation kinetics of MG oxidation and evaluate the evolution of main product, a chemical kinetic model was constructed. The model is based on the comprehensive chemical reaction networks, which include all elementary reactions, branching pathways, and associated rate constants derived from our quantum chemical calculations (detailed in SI). The concentration profiles of major intermediates and products were described by a system of coupled ordinary differential equations (ODEs) based on the law of mass action (Hoops et al., 2016; Muhammad et al., 2023; Thöni et al., 2025). For barrierless unimolecular decomposition reactions (e.g., k-RO_2H-1 → k-RO-1 + OH), a pre-exponential factor of $1.0 \times 10^{13}\ s^{-1}$ was adopted, approximately representing the typical Herzfeld's limiting rate of $6.21 \times 10^{12}\ s^{-1}$ according to the formula $k_H = k_B T/h$ (Campbell and Mao, 2021; Zhang et al., 2024). This system of ODEs was numerically integrated using the *solve_ivp* function from the SciPy (Virtanen et al., 2020) library (v1.6.2) in Python (v3.8) (Mate-Kole et al., 2023). The '*Radau*' implicit solver was employed, as it is specifically designed for stiff kinetic systems. To ensure numerical stability and prevent negative concentrations in trace intermediates, stringent error tolerances were set (relative tolerance $rtol = 1 \times 10^{-6}$ and absolute tolerance $atol = 1 \times 10^{-20}$). Simulations were run for a total duration of 60 min under conditions representative of aqueous aerosols. Separate simulations were conducted for the degradation kinetics of each MG hydrate (ADL, KDL, and TL), in order to evaluate the individual contribution to the formation of the corresponding products. The initial concentration of the primary reactant was set to 30 μM, and the concentration of dissolved O_2 was set to 2.5×10^{-4} M. A hydroxyl radical concentration of 10^{-15} - 10^{-8} M was considered to assess the sensitivity of the oxidation kinetics, and an initial concentration of 1.0×10^{-12} M was adopted, representing upper bound of cloud water (Ervens et al., 2014; Lallement et al., 2018).

3. Results and discussion

3.1. Initial reactions of MG with OH radical

For MG, the transformations in aerosol liquid, including oxidation with OH and hydration, were firstly investigated. As discussed in SI, MG oxidation pathways exhibit energy barriers ($\Delta G^{\ddagger}$) of 7.0 ~16.2 kcal mol^{-1} (Fig. S1), and the corresponding rate constants are less than $4.61 \times 10^7\ M^{-1}\ s^{-1}$. However, acid-catalyzed hydration (Fig. S2) forming hydrates is barrierless, with larger rate constants of $\sim 10^9\ M^{-1}\ s^{-1}$. It indicates the favorable hydrate formation for MG, in line with the available experimental evidence of 56~62% for diols (DLs) and 38~44% for tetrol (TL) (Nemet et al., 2004). Hence, the oxidation of MG in aqueous phase proceeds from DLs and TL. Fig. S3 shows the optimized geometries of DLs and TL at the M06-2X/6-311G(d,p) level. The potential energy surfaces (PESs) for possible pathways of the OH-initial reactions are depicted in Fig. 1. There are two distinct pathways for DLs, i.e., H-abstraction (R_{abs}) and OH-addition (R_{add}), but only H-abstraction (R_{abs}) for TL due to its saturated structure.

For aldehyde-DL (ADL), the H-abstraction pathways from the methyl group (a-$R_{abs}1$) and aldehyde-C site (a-$R_{abs}2$) possess the $\Delta G^{\ddagger}$ of 13.0 and 9.4 kcal mol^{-1}, respectively, which are at least 0.7 kcal mol^{-1} smaller than that of OH-addition to the aldehyde-C position (a-$R_{add}1$). Similarly, the $\Delta G^{\ddagger}$ values of the two H-abstraction pathways (k-$R_{abs}1$ and k-$R_{abs}2$) for ketone-DL (KDL) are at least 5.0 kcal mol^{-1} smaller than that of k-$R_{add}1$ pathways. It implies that for DLs, the H-abstraction pathways are thermodynamically more favorable than OH-addition pathways. As for TL, the H-abstraction from the methyl groups (t-$R_{abs}1$) possesses a lower $\Delta G^{\ddagger}$ value with 2.7 kcal mol^{-1} relative to that from the diol-C sites of TL (t-$R_{abs}2$). It indicates that for ADL, KDL, and TL, the R_{abs} pathways from non-methyl sites (i.e., diol-C and aldehyde-C sites) are thermodynamically more favorable than those from methyl groups. To evaluate the occurrence for H-abstraction, the bond dissociation energies (D^0_{298}(C–H)) of different H-abstraction sites were calculated at the M06-2X//M06-2X level. The D^0_{298}(C–H) values are 84.5 kcal mol^{-1} for the aldehyde-C site of ADL, 70.7 kcal mol^{-1} for the diol-C site of KDL, and 88.1 kcal mol^{-1} for the diol-C site of TL (Fig. S4). These D^0_{298}(C–H) values are at least 6.0 kcal mol^{-1} smaller than those of the corresponding methyl groups, indicating that the H atoms at the diol-C (a- and k-$R_{abs}2$) and aldehyde-C sites (t-$R_{abs}2$) are more reactive. Considering the energy barrier trend, the reactivity of the H atom in the two groups is dominantly affected by bond dissociation energies.

Fig. 2 depicts the calculated rate constants (k) and the branching ratios (Γ) for the OH-initial reaction pathways of ADL, KDL, and TL within the temperature range of 273 to 313 K. The lower bound represents the freezing point of water and the upper bound covers warmer conditions during summer or in tropical regions. For DLs, the H-abstraction pathways exhibit larger rate constants than those of OH-addition pathways at 298 K. For example, the calculated k values are 5.84×10^3 and $1.77 \times 10^9\ M^{-1}\ s^{-1}$ for a-$R_{abs}1$ and a-$R_{abs}2$, respectively, and 3.70×10^3 and $1.61 \times 10^6\ M^{-1}\ s^{-1}$ for k-$R_{abs}1$ and k-$R_{abs}2$, respectively, which are by 3 to 1000 times higher than those of the corresponding R_{add} pathways (a-$R_{add}1$ and k-$R_{add}1$). The R_{add} pathways exhibit Γ values of less than 0.1% (Table S1), implying the minor importance of R_{add} pathways to the total rate constants (i.e., the sum of rate constants for all reaction pathways). For TL, the k values are estimated to be 9.13×10^4 and $8.65 \times 10^6\ M^{-1}\ s^{-1}$ for t-$R_{abs}1$ and t-$R_{abs}2$, respectively. The evaluated Γ values of larger than 98% suggest that the

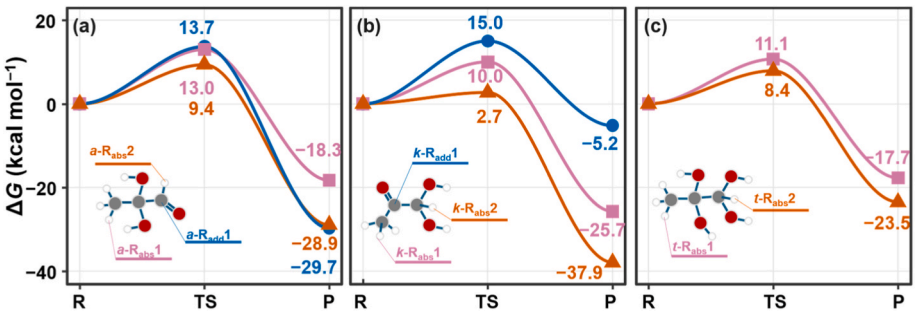

Fig. 1. PESs for the OH-initial reactions of (a) ADL, (b) KDL, and (c) TL.

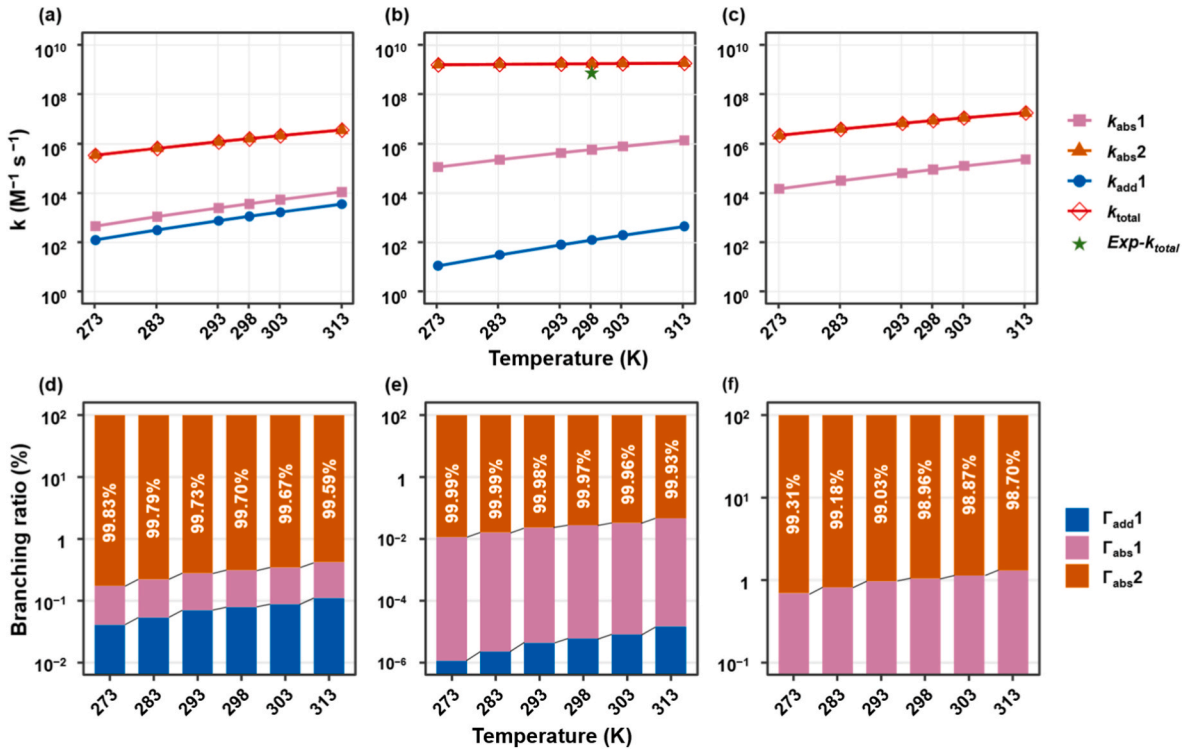

Fig. 2. (a-c) Rate constants and (d-f) branching ratios for the OH-initiated reactions of ADL (a, d), KDL (b, e), and TL (c, f) over 273 to 313 K.

H-abstraction pathways from non-methyl sites (*a*-, *k*-, and *t*-$R_{abs}2$) dominate the OH-initial reactions of ADL, KDL, and TL, producing alkyl radicals (*a*-, *k*-, and *t*-AR1) as key intermediates.

The temperature dependences of Γ were assessed within the temperature range of 273 to 313 K. As shown in Fig. 2d–f, the Γ values of *a*-, *k*-, and *t*-$R_{abs}2$ are greater than 99.0% in this range. It suggests that H-abstraction from non-methyl sites exhibits the predominant role in the OH-initial reactions of ADL, KDL, and TL. In addition, the total rate constants for the OH-initiated oxidation of KDL, TL and ADL at 298 K are 1.77×10^9, 8.74×10^6, and $1.61 \times 10^6\ M^{-1}\ s^{-1}$, respectively, corresponding to the ratio of about 1: 0.005: 0.001. The total rate constant of three MG hydrates is $1.78 \times 10^9\ M^{-1}\ s^{-1}$, consistent with the rate constant of $(1.1 \pm 0.1) \times 10^9\ M^{-1}\ s^{-1}$ measured by Ervens et al. (2003). Hence, the M06-2X//M06-2X method is reliable for the kinetic evaluation of the aqueous oxidation of MG. The Arrhenius expressions for the reactions of ADL, KDL, and TL with OH are derived to be 3.35×10^{13} exp $(-5021/T)$, 5.08×10^9 exp$(-314/T)$, and 3.26×10^{13} exp$(-45098/T)$ $M^{-1}\ s^{-1}$, respectively. The apparent activation energies are evaluated to

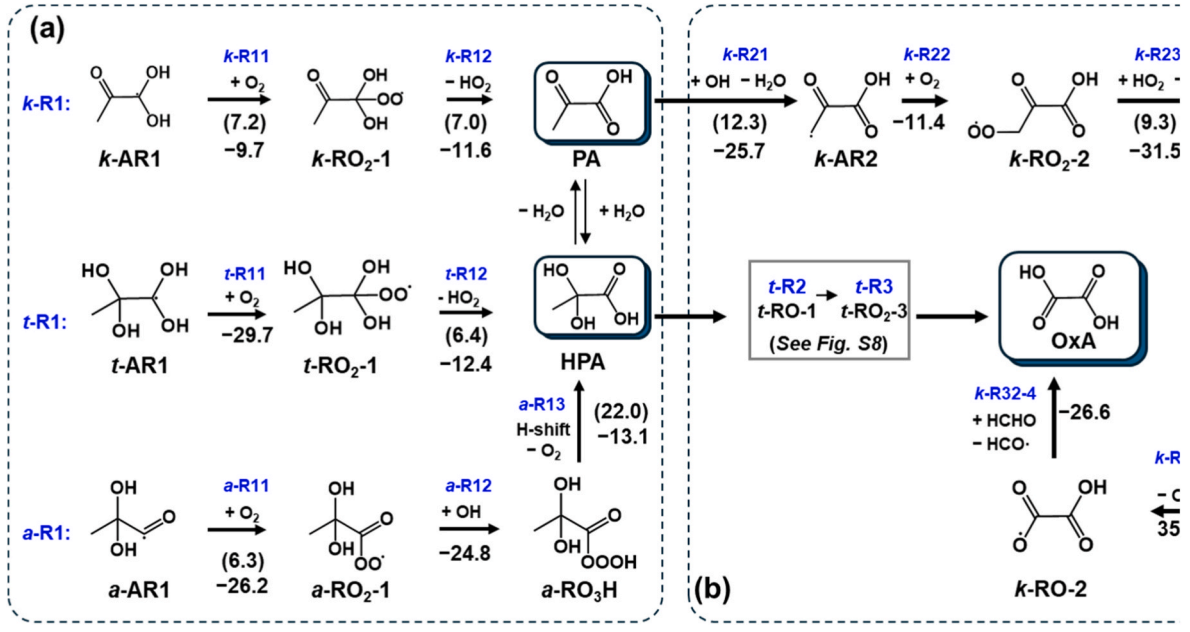

Fig. 3. Reaction pathways and energy profiles for the subsequent reactions of OH-initiated intermediates *a*-, *k*-, and *t*-AR1. (a) Formation of first-generation organic acids, (b) subsequent oxidation processes, and (c) competing formation of second-generation organic acids. The numbers aside arrows denote the $\Delta G^{\ddagger}$ (in brackets) and ΔG_r values for each unit reaction. Bold arrows indicate preferred pathways, and species in boxes are consistent with experimental detections.

be 10.0, 0.6, and 9.0 kcal mol^{-1} for the OH-initial reactions of ADL, KDL, and TL, respectively, suggesting that KDL exhibits the most favorable preference for OH-initial reactions.

3.2. Subsequent reactions of intermediates

Alkyl radicals (*a*-, *k*-, and *t*-AR1), as the dominant intermediates, are attacked by O_2 to yield peroxy radicals (*a*-, *k*-, and *t*-RO_2-1), which subsequently proceed via the following multistep processes (Fig. 3a),

k-R1 : k-AR1 $\xrightarrow{k\text{-R11:}+O_2}$ **k-TS11** → k-RO_2-1 $\xrightarrow{k\text{-R12:-}HO_2}$ **k-TS12** → PA

t-R1 : t-AR1 $\xrightarrow{t\text{-R11:}+O_2}$ t-RO_2-1 $\xrightarrow{t\text{-R12:-}HO_2}$ **t-TS12** →

a-R1 : a-AR1 $\xrightarrow{a\text{-R11:}+O_2}$ **a-TS11** → a-RO_2-1 $\xrightarrow{a\text{-R12:}+OH}$ a-RO_3H $\xrightarrow{a\text{-R13:}-O_2}$ **a-TS13** → HPA

For the O_2-addition to *t*-AR1 (pathway *t*-R11), no TS is identified and the barrierless nature of the pathway was further confirmed in Fig. S5. As shown in Fig. 3a, except the *t*-R11 pathway, the other two O_2-addition pathways (*k*-R11 and *a*-R11) exhibit the $\Delta G^{\ddagger}$ values of 7.2 and 6.3 kcal mol^{-1}, respectively. The estimated rate constants are in the range from ~10^7 to ~10^9 M^{-1} s^{-1} for the *a*-, *k*-, and *t*-R11 pathways (Tables S2–S4). Analysis of structures from Fig. S6 shows that *k*- and *t*-RO_2-1 possess the α-hydroxyl groups, leading to the distinct subsequent pathways compared with *a*-RO_2-1. The unimolecular HO_2-elimination of *k*-RO_2-1 and *t*-RO_2-1 (*k*-R12 and *t*-R12) form organic acids, i.e., pyruvic acid (PA) and 2,2-dihydroxypropanoic acid (HPA), with the $\Delta G^{\ddagger}$ values of 7.0 and 6.4 kcal mol^{-1}, respectively. The estimated rate constants of *k*-R12 and *t*-R12 pathways are 4.61×10^7 s^{-1} and 1.27×10^8 s^{-1}, respectively. However, *a*-RO_2-1 yields trioxide (*a*-RO_3H) rather than pyruvic acid because of no H-atoms at the α-position for HO_2-elimination. The reaction of *a*-RO_2-1 with OH radical (*a*-R12) is barrierless with the ΔG_r value of −24.8 kcal mol^{-1}. The following intramolecular H-shift of *a*-RO_3H is accompanied with O_2-elimination (*a*-R13), with the $\Delta G^{\ddagger}$ and ΔG_r values of 22.0 and −13.1 kcal mol^{-1}, respectively. It is evident from Fig. S6 that the same product, i.e., HPA is yielded from *a*-R1 and *t*-R1 pathways, suggesting that PA and HPA are the dominant products.

Subsequently, the reactions from PA to form alkoxy radical involve the following stepwise processes,

***k*-R2** : PA $\xrightarrow{k\text{-R21:}+OH}$ ***k*-TS21** → k-AR2 $\xrightarrow{k\text{-R22:}+O_2}$ *k*-RO_2-2

$\xrightarrow{k\text{-R23:}+HO_2}$ ***k*-TS23** → *k*-RO_2H-1 $\xrightarrow{k\text{-R24:}-OH}$ *k*-RO-1

As shown in Fig. 3b, the H-abstraction (*k*-R21) occurs at the methyl group of PA with the $\Delta G^{\ddagger}$ value of 12.3 kcal mol^{-1}, followed by the barrierless O_2-addition to form *k*-RO_2-2, which accepts the H-atom transferred from HO_2 (*k*-R23) by overcoming a TS with the $\Delta G^{\ddagger}$ value of 9.3 kcal mol^{-1}. Subsequent OH-elimination of *k*-RO_2H-1 (*k*-R24) is barrierless, forming alkoxy radical (*k*-RO-1). For *k*-RO-1, two distinct pathways are identified, H-abstraction (*k*-R31) at the methylene position (Fig. S7) and decomposition (*k*-R32, Fig. 3b). *k*-R32 pathway involves the elimination of formaldehyde (HCHO) and exhibits the smaller $\Delta G^{\ddagger}$ value of 7.0 kcal mol^{-1} than that of *k*-R31 pathway, forming alkyl radical (*k*-AR3). A kinetic analysis was conducted and discussed (details in SI, Table S5), showing that the branching ratio for *k*-R32 pathway exceeds 99%. Hence, we focus on the subsequent oxidation of *k*-AR3, which involves the following multistep reactions,

***k*-R3** : *k*-AR3 $\xrightarrow{k\text{-R32-1:}+O_2}$ *k*-RO_2-3 $\xrightarrow{k\text{-R32-2:}+HO_2}$ ***k*-TS32**-2 → *k*-RO_2H-2 $\xrightarrow{k\text{-R32-3:}-OH}$

k-RO-2 $\xrightarrow{k\text{-R32-4:}+HCHO}$ ***k*-TS32**-4 → OxA

Attack of *k*-AR3 (*k*-R32-1) by O_2 to form peroxy radicals (*k*-RO_2-3) is barrierless and exothermic, with the ΔG_r values of −26.4 kcal mol^{-1} (Fig. 3b). For peroxy radical *k*-RO_2-3 without H-atom at the α-position, the transformation proceeds via H-transfer from HO_2 (*k*-R32-2), OH-elimination (*k*-R32-3), and H-transfer from HCHO (*k*-R32-4). As shown in Fig. 3b, the *k*-R32-2 pathway to form *k*-RO_2H-2 exhibits the $\Delta G^{\ddagger}$ value of 9.4 kcal mol^{-1}, and *k*-R32-3 pathway to form *k*-RO-2 and *k*-R32-4 pathway to form OxA are barrierless, with the ΔG_r values of 35.0 and −26.6 kcal mol^{-1}, respectively.

Similarly, as discussed in SI, HPA also undergoes *t*-R2 and *t*-R3 pathways (Fig. S8) to ultimately form OxA. However, given the low initial rate constants of ADL and TL oxidation, organic acid formation via HPA is of minor importance in the atmosphere. These results suggest that the overall product distribution is regulated by oxidation of KDL to PA and its derivatives.

3.3. Reaction dynamics of organic acid formation

We performed a system of ordinary differential equations (ODEs) to evaluate the reaction kinetic simulation of reactant degradation and organic acid formation based on the chemical reaction network (Tables S6–8), which was described by combining the reaction processes and rate constants of each involved reaction obtained above. As shown in Fig. S9, ADL and TL exhibit a negligible degradation at the [OH] levels below 10^{-12} M, whereas KDL undergoes a significant degradation starting from [OH] levels of 10^{-14} M. It indicates that the oxidation of KDL is of major importance within the typical atmospheric [OH] range of 10^{-14} to 10^{-12} M. Fig. S10 depicts the concentration changes of ADL, KDL, and TL after 60 min OH-initiated degradation at the OH concentration of 10^{-12} M. The consumption (η) of ADL, KDL, and TL is evaluated according to the formula $\eta = \frac{C_0 - C}{C_0} \times$ 100%, where C and C_0 represent the final and initial concentrations of reactants, respectively. Under typical atmospheric conditions, the calculated η value is 99.8% for KDL, which is much larger than those of ADL and TL (<2%). It indicates that although rapid hydration equilibrium exists in the aqueous phase, the formation of organic acids in the MG oxidation system is primarily attributable to KDL.

Fig. 4a shows the dynamics of KDL concentration and its organic acid products during the oxidation process. Half of initial concentration for KDL is observed at 6.60 min, in agreement with the calculated half-life ($t_{1/2}$) of 6.62 min according to the formula $t_{1/2} = \frac{\ln 2}{k[OH]}$ (details in SI

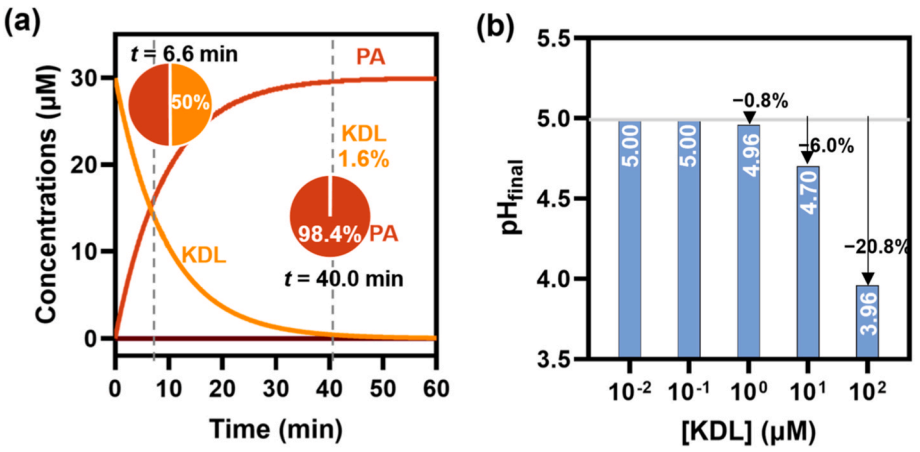

Fig. 4. Simulation for the organic acid formation kinetics: (a) precursor and product concentration dynamics of KDL oxidation and (b) microdroplet pH changes at various [KDL].

and Table S3). The consistency confirms the reliability of the ODE simulation in the description for the kinetic dynamics. During the simulation time (60 min), it is observed that there is a continuous accumulation of PA (red line in Fig. 4a) but a negligible formation of KPA and OxA, indicating that PA is the dominant organic acid product from the oxidation of MG. This finding is consistent with previous batch reactor study (Ortiz-Montalvo et al., 2016), which identified PA as the dominant organic acid produced during the aqueous oxidation of 5 μM MG. It can be attributed to the inhibition of further oxidation of PA, wherein the H-abstraction at the methyl group (*k*-R21) acts as the rate-limiting step due to the large $\Delta G^{\ddagger}$ (12.3 kcal mol^{-1}) and the low *k* value (1.81×10^{4} M^{-1} s^{-1}), as shown in Table S2. Therefore, we focus on the investigation of the role of PA on the microdroplet acidity in the following study.

We assumed an ideal microdroplet environment with an initial pH of 5 and with [OH] of 1×10^{-12} M, which represents an upper-limit estimate of acidity enhancement in the microdroplet. In this case, PA is expected to fully dissociate, yielding an equivalent concentration of protons. The final pH (pH_{final}) of microdroplet can be evaluated as a function of KDL concentration as follows:

$$pH_{final} = -\log([KDL] + 10^{-5})$$

Fig. 4b shows the pH_{final} of microdroplet as influenced by PA formation originating from different [KDL]. It can be found that the pH_{final} value of microdroplet is not affected if the [KDL] is less than the micromolar level (<1 μM). However, the microdroplet pH rapidly decreases if [KDL] is more than 1 μM. For example, the pH_{final} value is 3.96 with 100 μM KDL, corresponding to a 20.8% pH drop, which is more than three times larger than that with 10 μM KDL. Our current results suggest that considering the observed larger than micromolecular concentration in aerosols, the aqueous oxidation of MG significantly affects the microdroplet acidity, especially for the heavily polluted areas with higher concentration of MG.

4. Conclusions and atmospheric implications

In this study, we investigated the mechanisms and kinetics of the OH-initiated aqueous reaction of methylglyoxal (MG) using quantum chemical and reaction rate calculations, and further examined the

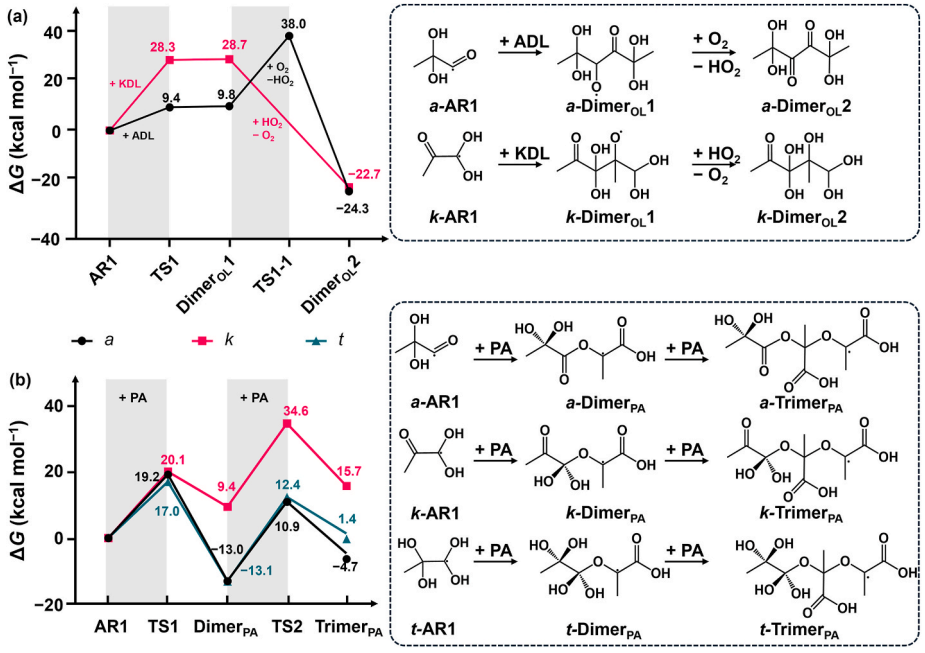

Fig. 5. Reaction pathways and potential energy surfaces for oligomerization of *a*-, *k*-, and *t*-AR1 with (a) ADL and KDL, and with (b) PA (in unit of kcal mol^{-1}).

product yields through reaction dynamic simulations. We found that the direct oxidation of MG is hindered because of large energy barriers and small rate constants relative to barrierless hydration of MG to form hydrates. The OH-initiated reactions of MG hydrates such as diols (ADL and KDL) and tetrol (TL) mainly proceed via H-abstraction pathways, which exhibit lower energy barriers and higher rate constants than OH-addition. Our kinetic results reveal that H-abstraction from non-methyl sites is favored over 273 to 313 K, yielding alkyl radicals (*a*-, *k*-, and *t*-AR1) with the branching ratios more than 98%. Subsequent reactions produce pyruvic acid (PA) from *k*-AR1 in the presence of O_2, and form 2,2-dihydroxypropanoic acid (HPA) from *a*- and *t*-AR1. Further oxidation of PA and HPA proceeds via a series of pathways, such as H-abstraction, O_2-addition, H-transfer, OH-elimination, and decomposition, ultimately leading to the formation of oxalic acid (OxA), as a common final product of the OH-initiated oxidation of MG.

Reaction dynamic simulations demonstrate that the MG oxidation is mainly contributed by KDL under typical aerosol conditions ($[OH] = 10^{-12}$ M). PA is the primary product of KDL oxidation in the aerosol phase and is accumulated throughout the simulation. We also evaluated the influence of MG oxidation on aerosol acidity, which shows that the microdroplet acidity is substantially decreased by the formation of PA when KDL concentration is larger than micromolecular level. Moreover, the effect of initial microdroplet acidity was examined and is shown in Fig. S11. The oxidation of 100 μM KDL leads to an approximately 33% pH decrease in a microdroplet with an initial pH of 6, more than 1.5 times the decrease observed for a microdroplet with an initial pH of 5. Hence, the microdroplet acidity enhancement is more sensitive to the initial acidity and exerts a greater impact under less acidic conditions.

On the other hand, the competing reaction for the formation of oligomers was also evaluated. In the MG oxidation system, oligomerization can be initiated by alkyl radicals, which proceeds via three distinct pathways (Fig. 5 and Fig. S12): (i) self-oligomerization, (ii) reaction with the main organic acid product (PA), and (iii) reaction with unsaturated diols (ADL and KDL). Due to the high energy barriers, oligomers do not originate from the reactions of alkyl radicals with DLs and PA, but instead form from alkyl radicals themselves (Fig. S12). However, when the concentration of alkyl radical is less than 10^{-4} M, the self-oligomerization of alkyl radicals exhibits a lower reaction rate than that of O_2-addition to form organic acids (Fig. S13). Therefore, further oxidation toward organic acids rather than oligomer formation dominates the MG oxidation under atmospheric aqueous conditions. This work provides mechanistic and kinetic insights into the aqueous-phase oxidation of MG and reveals its key role in the formation of low-molecular-weight organic acids. These findings underscore the importance of aqueous-phase oxidation of OVOCs in influencing aerosol acidity and composition.

CRediT authorship contribution statement

Jiaxin Wang: Formal analysis, Investigation, Methodology, Visualization, Writing – original draft. **Ying Chen:** Conceptualization, Formal analysis, Investigation, Validation. **Wenjie Gao:** Formal analysis, Investigation. **Sihao Lin:** Formal analysis, Writing – review & editing. **Wenjian Li:** Writing – review & editing. **Yongpeng Ji:** Writing – review & editing. **Xiaolei Zhao:** Writing – review & editing. **Yanpeng Gao:** Supervision. **Yuemeng Ji:** Supervision, Validation, Writing – review & editing. **Taicheng An:** Supervision.

Declaration of competing interest

The authors declare that they have no known competing financial interests or personal relationships that could have appeared to influence the work reported in this paper.

Acknowledgements

This work was financially supported by National Natural Science Foundation of China (42020104001, U25A20825, 42577431, and 42077189), Guangdong Basic and Applied Basic Research Foundation (2025A1515011379), Technology Elite Navigation Project of Guangzhou (2025A04J7038), and Guang-dong Provincial Key R&D Program (2022-GDUT-A0007).

Appendix A. Supplementary data

Supplementary data to this article can be found online at https://doi.org/10.1016/j.atmosenv.2026.121896.

Data availability

Data will be made available on request.

References

Campbell, C.T., Mao, Z.T., 2021. Analysis and prediction of reaction kinetics using the degree of rate control. J. Catal. 404, 647–660.
Chan, K.M., Huang, D.D., Li, Y.J., Chan, M.N., Seinfeld, J.H., Chan, C.K., 2013. Oligomeric products and formation mechanisms from acid-catalyzed reactions of methyl vinyl ketone on acidic sulfate particles. J. Atmos. Chem. 70, 1–18.
Collins, F.C., Kimball, G.E., 1949. Diffusion-controlled reaction rates. J. Colloid Sci. 4, 425–437.
Degefie, D.T., El-Madany, T.S., Held, M., Hejkal, J., Hammer, E., Dupont, J.C., et al., 2015. Fog chemical composition and its feedback to fog water fluxes, water vapor fluxes, and microphysical evolution of two events near Paris. Atmos. Res. 164, 328–338.
Ervens, B., Gligorovski, S., Herrmann, H., 2003. Temperature-dependent rate constants for hydroxyl radical reactions with organic compounds in aqueous solutions. Phys. Chem. Chem. Phys. 5, 1811–1824.
Ervens, B., Sorooshian, A., Lim, Y.B., Turpin, B.J., 2014. Key parameters controlling OH-initiated formation of secondary organic aerosol in the aqueous phase (aqSOA). J. Geophys. Res. Atmos. 119, 3997–4016.
Evans, M.G., Polanyi, M.G., 1935. Some applications of the transition state method to the calculation of reaction velocities, especially in solution. Trans. Faraday Soc. 31, 1965–1967.
Eyring, H., 1935. The activated complex in chemical reactions. J. Chem. Phys. 3, 107–115.
Fröhlich-Nowoisky, J., Kampf, C.J., Weber, B., Huffman, J.A., Pöhlker, C., Andreae, M. O., et al., 2016. Bioaerosols in the Earth system: climate, health, and ecosystem interactions. Atmos. Res. 182, 346–376.
Frisch, M.J., Trucks, G.W., Schlegel, H.B., Scuseria, G.E., Robb, M.A., Cheeseman, J.R., et al., 2009. Gaussian 09, vol. 1. Revision D.
Fu, T.M., Jacob, D.J., Wittrock, F., Burrows, J.P., Vrekoussis, M., Henze, D.K., 2008. Global budgets of atmospheric glyoxal and methylglyoxal, and implications for formation of secondary organic aerosols. J. Geophys. Res. Atmos. 113.
Gao, Y., Ji, Y., Li, G., An, T., 2013. Mechanism, kinetics and toxicity assessment of OH-initiated transformation of triclosan in aquatic environments. Water Res. 49, 360–370.
Ge, M.F., Tong, S.R., Du, L., Wu, L.Y., Lei, T., Li, K., et al., 2025. The influence of heterogeneous processes on the physicochemical properties of atmospheric aerosols. Adv. Atmos. Sci. 42, 623–640.
George, C., Ammann, M., D'Anna, B., Donaldson, D.J., Nizkorodov, S.A., 2015. Heterogeneous photochemistry in the atmosphere. Chem. Rev. 115, 4218–4258.
Hazra, M.K., Sinha, A., 2011. Formic acid catalyzed hydrolysis of SO_3 in the gas phase: a barrierless mechanism for sulfuric acid production of potential atmospheric importance. J. Am. Chem. Soc. 133, 17444–17453.
Henry, E., 1935. The activated complex and the absolute rate of chemical reactions. Chem. Rev. 17, 65–77.
Hoops, S., Hontecillas, R., Abedi, V., Leber, A., Philipson, C., Carbo, A., et al., 2016. Chapter 5 - ordinary differential equations (ODEs) based modeling. In: Bassaganya-Riera, J. (Ed.), Computational Immunology. Academic Press, pp. 63–78.
Ji, Y., Shi, Q., Li, Y., An, T., Zheng, J., Peng, J., et al., 2020. Carbenium ion-mediated oligomerization of methylglyoxal for secondary organic aerosol formation. Proc. Natl. Acad. Sci. USA 117, 13294–13299.
Ji, Y.M., Zhao, J., Terazono, H., Misawa, K., Levitt, N.P., Li, Y.X., et al., 2017. Reassessing the atmospheric oxidation mechanism of toluene (vol 114, pg 8169, 2017). Proc. Natl. Acad. Sci. USA 114, E8314. E8314.
Lallement, A., Vinatier, V., Brigante, M., Deguillaume, L., Delort, A.M., Mailhot, G., 2018. First evaluation of the effect of microorganisms on steady state hydroxyl radical concentrations in atmospheric waters. Chemosphere 212, 715–722.
Lelieveld, J., Pozzer, A., Pöschl, U., Fnais, M., Haines, A., Münzel, T., 2020. Loss of life expectancy from air pollution compared to other risk factors: a worldwide perspective. Cardiovasc. Res. 116, 1910–1917.
Li, F.H., Tang, S.S., Tsona, N.T., Du, L., 2020a. Kinetics and mechanism of OH-induced α-terpineol oxidation in the atmospheric aqueous phase. Atmos. Environ. 237.

Li, J., Ning, A., Liu, L., Zhang, X.H., 2024. Atmospheric bases-enhanced iodic acid nucleation: altitude-dependent characteristics and molecular mechanisms. Environ. Sci. Technol. 58, 16962–16973.
Li, T., Wang, Z., Wang, Y.R., Wu, C., Liang, Y.H., Xia, M., et al., 2020b. Chemical characteristics of cloud water and the impacts on aerosol properties at a subtropical mountain site in Hong Kong SAR. Atmos. Chem. Phys. 20, 391–407.
Lim, Y.B., Tan, Y., Perri, M.J., Seitzinger, S.P., Turpin, B.J., 2010. Aqueous chemistry and its role in secondary organic aerosol (SOA) formation. Atmos. Chem. Phys. 10, 10521–10539.
Lim, Y.B., Tan, Y., Turpin, B.J., 2013. Chemical insights, explicit chemistry, and yields of secondary organic aerosol from OH radical oxidation of methylglyoxal and glyoxal in the aqueous phase. Atmos. Chem. Phys. 13, 8651–8667.
Liu, X.D., Wu, C., Li, Z., Li, R.J., Wang, F.L., Lv, S.J., et al., 2024. Atmospheric brown carbon in China haze is dominated by secondary formation. Sci. Total Environ. 945.
Liu, Y., Siekmann, F., Renard, P., El Zein, A., Salque, G., El Haddad, I., et al., 2012a. Oligomer and SOA formation through aqueous phase photooxidation of methacrolein and methyl vinyl ketone. Atmos. Environ. 49, 123–129.
Liu, Z., Wang, Y.H., Vrekoussis, M., Richter, A., Wittrock, F., Burrows, J.P., et al., 2012b. Exploring the missing source of glyoxal (CHOCHO) over China. Geophys. Res. Lett. 39.
Ma, W., Zheng, F.X., Zhang, Y.S., Chen, X., Zhan, J.L., Hua, C.J., et al., 2022. Weakened gas-to-particle partitioning of oxygenated organic molecules in liquified aerosol particles. Environ. Sci. Technol. Lett. 9, 837–843.
Marenich, A.V., Cramer, C.J., Truhlar, D.G., 2009. Universal solvation model based on solute electron density and on a continuum model of the solvent defined by the bulk dielectric constant and atomic surface tensions. J. Phys. Chem. B 113, 6378–6396.
Marrero-Ortiz, W., Hu, M., Du, Z., Ji, Y., Wang, Y., Guo, S., et al., 2019. Formation and optical properties of brown carbon from small alpha-Dicarbonyls and amines. Environ. Sci. Technol. 53, 117–126.
Mate-Kole, E.M., Margot, D., Dewji, S.A., 2023. Mathematical solutions in internal dose assessment: a comparison of Python-based differential equation solvers in biokinetic modeling. J. Radiol. Prot. 43.
McNeill, V.F., 2015. Aqueous organic chemistry in the atmosphere: sources and chemical processing of organic aerosols. Environ. Sci. Technol. 49, 1237–1244.
Minerath, E.C., Casale, M.T., Elrod, M.J., 2008. Kinetics feasibility study of alcohol sulfate esterification reactions in tropospheric aerosols. Environ. Sci. Technol. 42, 4410–4415.
Muhammad, I., Makwashi, N., Ahmed, T.G., Manos, G., Zhao, D.L., 2023. A mechanistic model on catalyst deactivation by coke formation in a CSTR reactor. Processes 11.
Nemet, I., Vikic-Topic, D., Varga-Defterdarovic, L., 2004. Spectroscopic studies of methylglyoxal in water and dimethylsulfoxide. Bioorg. Chem. 32, 560–570.
Okuno, Y., 1997. Theoretical investigation of the mechanism of the baeyer-villiger reaction in nonpolar solvents. Chem. Eur J. 3, 212–218.
Ortiz-Montalvo, D.L., Schwier, A.N., Lim, Y.B., McNeill, V.F., Turpin, B.J., 2016. Volatility of methylglyoxal cloud SOA formed through OH radical oxidation and droplet evaporation. Atmos. Environ. 130, 145–152.
Powelson, M.H., Espelien, B.M., Hawkins, L.N., Galloway, M.M., De Haan, D.O., 2014. Brown carbon formation by aqueous-phase carbonyl compound reactions with amines and ammonium sulfate. Environ. Sci. Technol. 48, 985–993.
Sander, R., 2015. Compilation of Henry's law constants (version 4.0) for water as solvent. Atmos. Chem. Phys. 15, 4399–4981.
Schaefer, T., Schindelka, J., Hoffmann, D., Herrmann, H., 2012. Laboratory kinetic and mechanistic studies on the OH-Initiated oxidation of acetone in aqueous solution. J. Phys. Chem. A 116, 6317–6326.
Shi, Q.J., Gao, L., Li, W.J., Wang, J.X., Shi, Z., Li, Y.X., et al., 2024. Oligomerization mechanism of methylglyoxal regulated by the methyl groups in reduced nitrogen species: implications for brown carbon formation. Environ. Sci. Technol. 58, 1563–1576.
Tan, Y., Carlton, A.G., Seitzinger, S.P., Turpin, B.J., 2010. SOA from methylglyoxal in clouds and wet aerosols: measurement and prediction of key products. Atmos. Environ. 44, 5218–5226.
Tan, Y., Lim, Y.B., Altieri, K.E., Seitzinger, S.P., Turpin, B.J., 2012. Mechanisms leading to oligomers and SOA through aqueous photooxidation: insights from OH radical oxidation of acetic acid and methylglyoxal. Atmos. Chem. Phys. 12, 801–813.
Tan, Y., Perri, M.J., Seitzinger, S.P., Turpin, B.J., 2009. Effects of precursor concentration and acidic sulfate in aqueous Glyoxal-OH radical oxidation and implications for secondary organic aerosol. Environ. Sci. Technol. 43, 8105–8112.
Thöni, A.C.M., Robinson, W.E., Bachrach, Y., Huck, W.T.S., Kachman, T., 2025. Modeling chemical reaction networks using neural ordinary differential equations. J. Chem. Inf. Model. 65, 4346–4352.
Tilgner, A., Brauer, P., Wolke, R., Herrmann, H., 2013. Modelling multiphase chemistry in deliquescent aerosols and clouds using CAPRAM3.0i. J. Atmos. Chem. 70, 221–256.
Virtanen, P., Gommers, R., Oliphant, T.E., Haberland, M., Reddy, T., Cournapeau, D., et al., 2020. SciPy 1.0: fundamental algorithms for scientific computing in python. Nat. Methods 17, 261–272.
Wang, J.X., Ma, X.H., Ji, Y.M., Ji, Y.P., Gao, Y.P., Xiao, Y.Q., et al., 2023a. Competing esterification and oligomerization reactions of typical long-chain alcohols to secondary organic aerosol formation. J. Environ. Sci. 126, 103–112.
Wang, Y.C., Liang, S.M., Le Breton, M., Wang, Q.Q., Liu, Q.Y., Ho, C.H., et al., 2023b. Field observations of C2 and C3 organosulfates and insights into their formation mechanisms at a suburban site in Hong Kong. Sci. Total Environ. 904.
Wei, B., Zhang, R.F., Sit, P.H.L., He, M.X., Chan, C.K., 2023. Theoretical study on the aqueous phase oxidation of glyoxal. Environ. Sci. Atmosph. 3, 1296–1305.
Xu, T., Chen, J.W., Wang, Z.Y., Tang, W.H., Xia, D.M., Fu, Z.Q., et al., 2019. Development of prediction models on base-catalyzed hydrolysis kinetics of phthalate esters with density functional theory calculation. Environ. Sci. Technol. 53, 5828–5837.
Zhang, C.H., Kundu, S., Makri, N., Gruebele, M., Wolynes, P.G., 2024. Quantum information scrambling and chemical reactions. Proc. Natl. Acad. Sci. USA 121.
Zhang, R.Y., Wang, G.H., Guo, S., Zarnora, M.L., Ying, Q., Lin, Y., et al., 2015. Formation of urban fine particulate matter. Chem. Rev. 115, 3803–3855.
Zhang, X., Chen, Z.M., Zhao, Y., 2010. Laboratory simulation for the aqueous OH-oxidation of methyl vinyl ketone and methacrolein: significance to the in-cloud SOA production. Atmos. Chem. Phys. 10, 9551–9561.
Zhao, Q.J., Xie, H.B., Ma, F.F., Nie, W., Yan, C., Huang, D.D., et al., 2023. Mechanism-based structure-activity relationship investigation on hydrolysis kinetics of atmospheric organic nitrates. npj Clim. Atmos. Sci. 6.
Zhao, Y., Truhlar, D.G., 2008. The M06 suite of density functionals for main group thermochemistry, thermochemical kinetics, noncovalent interactions, excited states, and transition elements: two new functionals and systematic testing of four M06-class functionals and 12 other functionals. Theor. Chem. Acc. 120, 215–241.